International Journal of Microwave and Wireless Technologies

cambridge.org/mrf

X-band mechanical waveguide switch with gap waveguide technology and its actuator mechanism

Merve Güvenç[1], Çağlar Konak[2], İsmail Şişman[1,3] and A. Arif Ergin[4]

[1]Electrical and Electronic Engineering, Yeditepe University, Istanbul, Türkiye; [2]Physics, Middle East Technical University, Ankara, Türkiye; [3]R&D, Profen Communication Technologies, Istanbul, Türkiye and [4]Electrical and Electronics Engineering, Bahçeşehir University, Istanbul, Türkiye

Research Paper

Cite this article: Güvenç M, Konak Ç, Şişman İ, Ergin AA (2026) X-band mechanical waveguide switch with gap waveguide technology and its actuator mechanism. *International Journal of Microwave and Wireless Technologies* **18**(4), 572–582. https://doi.org/10.1017/S1759078726103638

Received: 14 October 2025 UTC
Revised: 29 June 2026 UTC
Accepted: 30 June 2026 UTC
First published online: 16 September 2026 UTC

Keywords:
actuating mechanism; gap waveguide technology; high power; switch; waveguide switch

Corresponding author: Merve Güvenç; Email: merve.guvenc@std.yeditepe.edu.tr

Abstract

The design of double-pole double-throw (DPDT) and single-pole double-throw (SPDT) waveguide switches, along with their actuating mechanisms for high-power applications, is presented. The mechanical waveguide switch is based on gap waveguide technology, which uses a controlled air gap to prevent electromagnetic wave leakage. A rotating inner cylinder enables signal transmission and switching, while a fixed outer cube protects the cylinder and secures the input and output ports. Dividing the switch into two parts simplifies manufacturing and assembly. The switch can withstand a peak power of 100 kW. Its electrical performance is analyzed using CST Studio Suite. The proposed switch is fabricated and experimentally validated, showing strong agreement between simulated and measured results. The return loss exceeds 30 dB, indicating very low reflected power, while the insertion loss is below 0.1 dB, demonstrating minimal signal power loss. The isolation is greater than 90 dB, indicating extremely low leakage between ports. The switching operation is controlled by an actuating mechanism designed using COMSOL Multiphysics. The mechanism operates at 28 V and 0.9 A, achieving a switching time of 50 ms. The proposed design provides high-power handling capability, low loss, high isolation, and fast switching performance.

Introduction

High-frequency communication and radar systems demand efficient, low-loss transmission lines capable of handling high power levels. Conventional rectangular waveguides are widely used in such applications due to their superior power handling and low-loss characteristics. However, the requirement for metal-to-metal contact in traditional waveguide assemblies often increases complexity and reduces long-term reliability.

Gap waveguide technology (GWT), proposed as an alternative to conventional designs, enables contactless wave propagation by introducing periodic pin structures between parallel conducting plates. These periodic structures create a stopband that suppresses unwanted modes, allowing electromagnetic waves to propagate only in desired paths [1–5]. GWT has found applications in a variety of high-frequency components, such as filters, antennas, and couplers, as well as in packaging techniques [6–13], where ease of fabrication and assembly without electrical contact is particularly advantageous.

Waveguide switches are essential for systems that require signal routing, including radar front ends, satellite payloads, and RF test systems. Mechanical waveguide switches, in particular, are favored for high-power applications due to their robustness, low insertion loss, and high isolation. Although several studies have explored the use of GWT in switch designs [14–19], they are typically limited in configurability, integration with actuation systems, or power handling capabilities.

This work presents the design and implementation of a novel mechanical waveguide switch operating in the X-band (8.2–12.4 GHz) that utilizes GWT for contactless, low-loss operation. The switch supports both double-pole double-throw (DPDT) and single-pole double-throw (SPDT) configurations and can withstand up to 100 kW of peak power. It consists of a rotatable inner cylinder enclosed in a stationary outer cube, with a non-contact interface that leverages GWT principles. Additionally, a compact rotary actuator mechanism is developed and integrated into the system, enabling reliable switching within 50 ms.

© The Author(s), 2026. Published by Cambridge University Press in association with The European Microwave Association. This is an Open Access article, distributed under the terms of the Creative Commons Attribution licence (http://creativecommons.org/licenses/by/4.0), which permits unrestricted re-use, distribution and reproduction, provided the original article is properly cited.

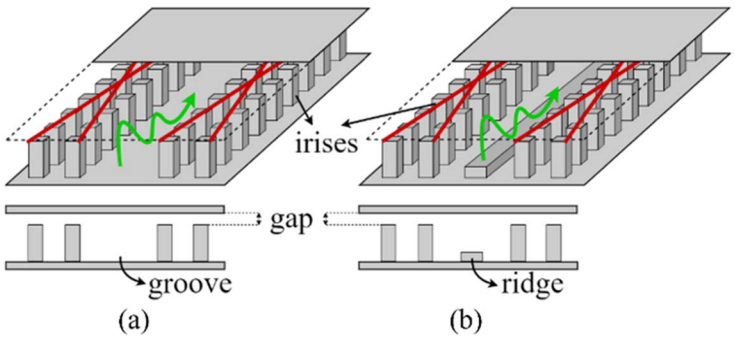


Figure 1. Gap waveguide geometries and signal propagation. (a) Groove gap waveguide. (b) Ridge gap waveguide.

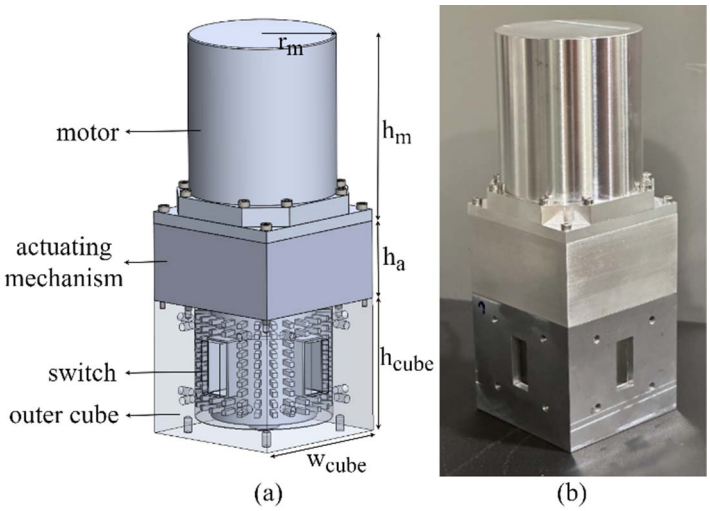


Figure 2. Outer structure. (a) Design model. (b) Fabricated model.

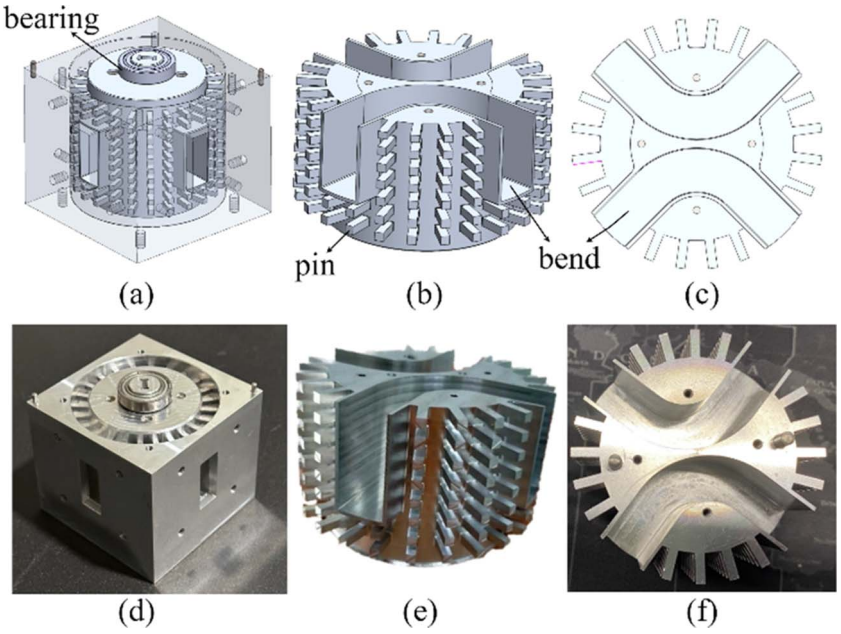


Figure 3. Inner cylinder. (a–c) Design model. (d–f) Production model.

https://doi.org/10.1017/S1759078726103638 Published online by Cambridge University Press

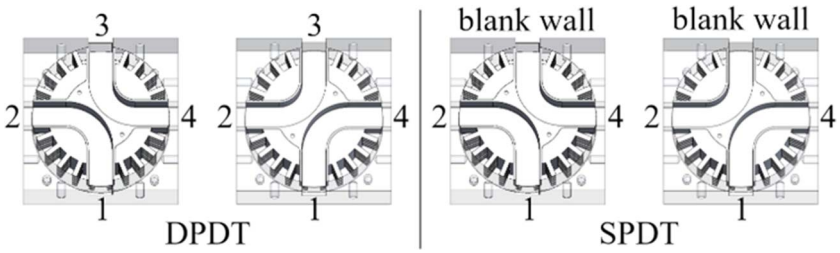


Figure 4. Switching configurations for DPDT and SPDT.

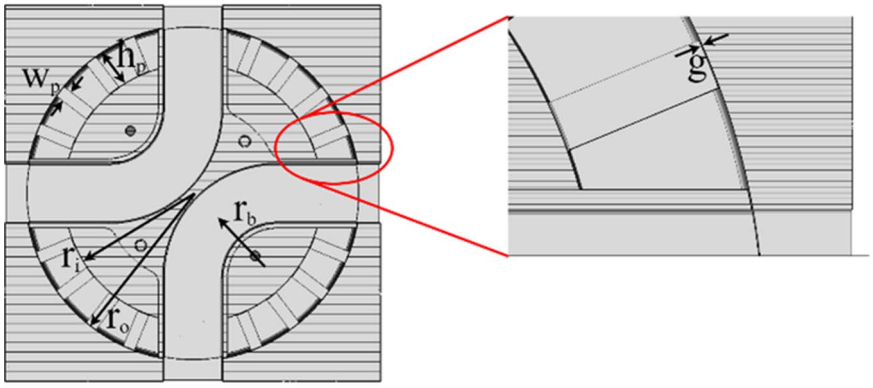


Figure 5. Dimensions of the parts of the inner cylinder.

The main contribution of this work is the development of a fully integrated high-power waveguide switch that combines GWT with a custom-designed rotary actuator. The design simplifies manufacturing through its contactless interface, enhances electrical performance through optimized geometric parameters, and ensures safe operation at high power levels via detailed RF breakdown simulations. The switch's performance is validated by electromagnetic and mechanical simulations and experimental measurements, with strong agreement across the full X-band.

The gap waveguide technology

The concept of a gap waveguide is based on controlling the propagation of an electromagnetic wave in a waveguide with parallel plates, allowing it to propagate only in desired directions, using the fundamentals of boundary conditions and canonical surfaces. Pins are periodically placed on only one of the plates with a gap between the pins and the other plate (Fig. 1). In this way, the signal is transmitted between two plates that are not in contact with each other. This enables control of signal transmission and limits unwanted signal propagation between two contactless plates, making it easier to manufacture and combine the plates than their conventional counterparts.

Figure 1 shows two GWT configurations and their corresponding signal transmission paths. In GWT, pins placed on one of the metal plates can serve as a bed of nails, but they can also be designed in different periodic shapes [20, 21]. Periodic structures create a high impedance for surface waves. The wave cannot propagate in this region. To create the stopband for the wave, the gap between the plate and the pins must be smaller than the signal's quarter wavelength (λ/4). To create a propagation path for the waves, the space between the pins is left empty (Fig. 1(a)) or a metal plate is placed (Fig. 1(b)). These are called the groove-gap waveguide and the ridge-gap waveguide, respectively [22, 23]. The signal travels in the space between the plates or the space between the ridge and the other plate.

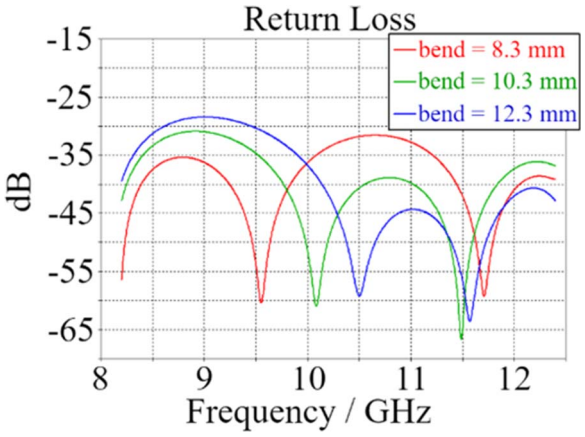


Figure 6. Return loss for different bend radii.

Switch design

The waveguide switch consists of an inner cylinder and an outer cube, manufactured separately. The inner cylinder is placed inside the outer cube using the shrink-fit method. The electromagnetic simulations of the waveguide switch were performed using CST Studio Suite (Dassault Systèmes) [24].

The outer cube

Four WR90 ports are placed on the side surfaces of the stationary outer cube. There is a 90° angle between the ports on the horizontal axis. The outer cube is designed as a shell for the motor, actuating mechanism, and switch. The outer cube is connected to the inner cylinder via bearings at the top and bottom. Inside the outer cube, there is a cavity in which the inner cylinder is positioned and rotates. The radius of this cavity is larger than the radius of the inner cylinder, so that the inner cylinder can rotate easily inside the outer

https://doi.org/10.1017/S1759078726103638 Published online by Cambridge University Press

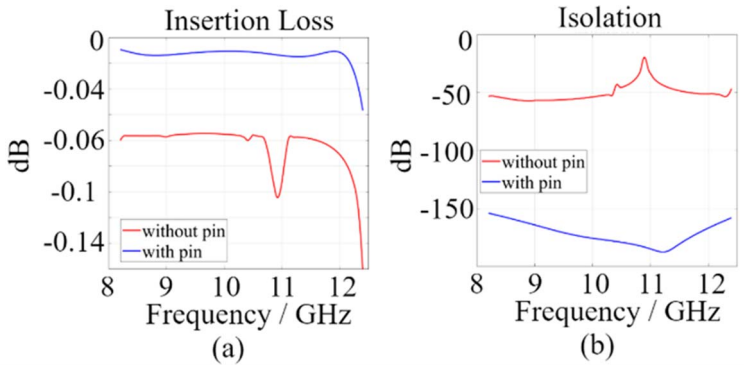


Figure 7. (a) Insertion and (b) isolation with pin and without pin.

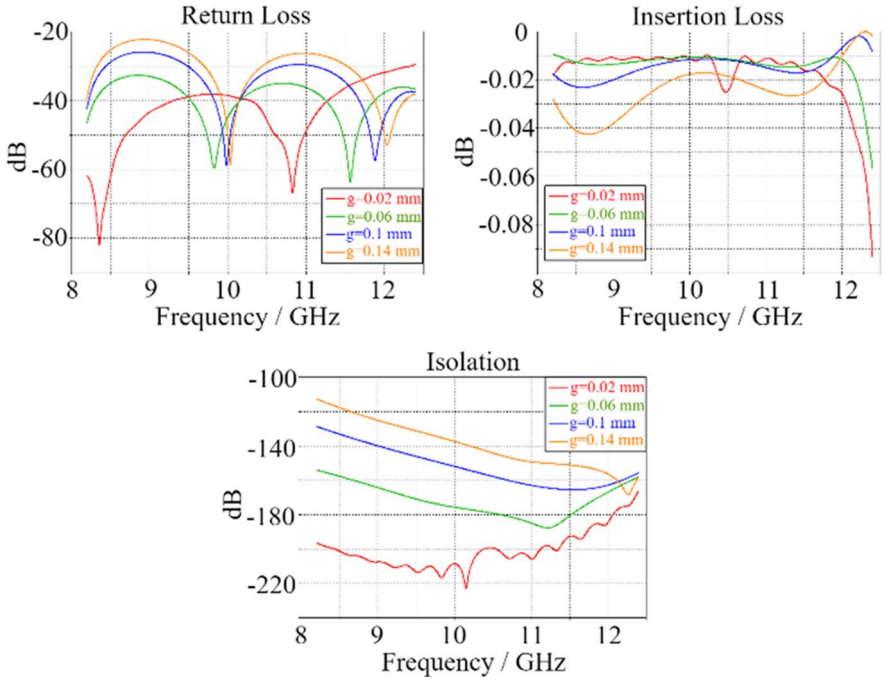


Figure 8. Insertion loss, return loss, and isolation for different gap values.

cylinder. Ports on the outer cube transmit the signal to the switch. Switching occurs when the inner cylinder is rotated 90° while the outer cylinder remains stationary. For switching, the motor located at the top of the outer cube drives the actuating mechanism, which rotates the inner cylinder.

The design and fabricated models for the outer cube structure are given in Fig. 2.

The inner cylinder

The inner cylinder contains two signal transmission paths, each consisting of a 90° bend WR90 waveguide. Rotating the inner cylinder by 90° changes the ports to which the waveguides are connected, and switching takes place. The rotation of the inner cylinder is provided by the bearings located at the top and bottom. The bends and bearings in the inner cylinder are shown in Fig. 3. Figure 3(a)–(c) shows the design models, while Fig. 3(d)–(f) shows the production models.

A DPDT waveguide switch is one in which two inputs and two outputs are controlled. If one of the ports is set to a blank wall, the switch operates in SPDT mode. The switching configurations for DPDT and SPDT are shown in Fig. 4.

The signal that reaches the switch via the port on the outer cube must travel through the bend structure on the inner cylinder. However, the inner cylinder and the outer cube are separate parts, with a gap between them. The GWT is used to prevent the signal from leaking through this gap. The square pin arrays on the inner cylinder's side surface are designed to be periodic. The pins create a high impedance on the inner cylinder's side surface. Thus, the signal continues to travel along the bend instead of leaking through the gap between the outer cube and the inner cylinder. The design parameters that affect the leakage amount are the gap size between the inner cylinder and the outer cube, g, the pin sizes (width, w_p, and height, h_p), the gap between the pins (g_p), and the radii (r_i and r_o) of the inner cylinder as depicted in Fig. 5.

In a waveguide switch, the insertion loss between two ports with a bend connection is expected to be as low as possible (close to zero). On the other hand, return loss at each input port is expected to be high.

The bend radius (r_b) affects the return loss. Figure 6 shows a plot of the simulated return loss for only a change in the bend radius values. In this design, the bend radius where the return loss is the best is 8.3 mm.

https://doi.org/10.1017/S1759078726103638 Published online by Cambridge University Press

Table 1. Design parameters of the waveguide switch

Parameter	Value (mm)
h_{cube}	55.7
w_{cube}	63.9
h_p	6.5
w_p	2
r_i	21.9
r_o	28.4
r_b	8.3
g	0.06

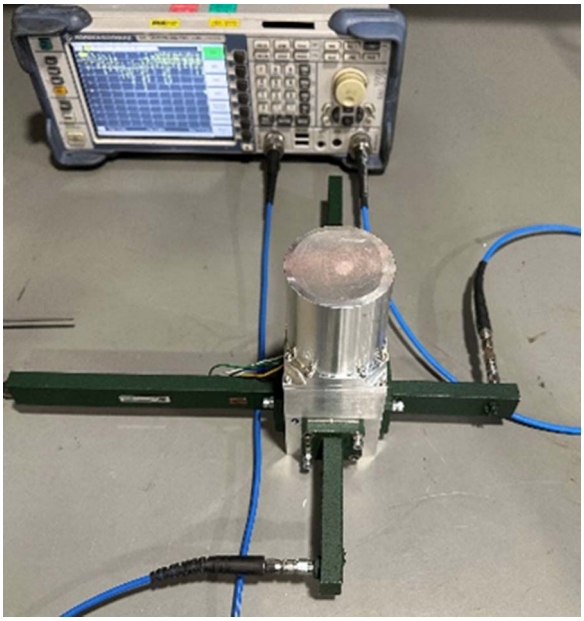


Figure 9. Measurement setup of the waveguide switch.

In a waveguide switch, the isolation between the ports that are not connected via a waveguide is expected to be high. Pins provide isolation by preventing wave leakage through the gap between the inner and outer structures. Figure 7 shows the effect of the design with and without pins (all pins are removed from the structure) on insertion loss and isolation. When the pins on the structure are removed, the insertion loss increases from a maximum of 0.05–0.15 dB. Likewise, the isolation value decreases from a minimum of 150–20 dB. The peak observed when the pins are removed is caused by electromagnetic leakage into the gap between the inner cylinder and the outer cube, where the gap region behaves as a resonant cavity at that frequency.

The gap between the outer cube and the rotating inner cylinder is a parameter that directly affects all results. A small gap improves return loss, insertion loss, and isolation. However, the inner cylinder structure needs space to rotate inside the outer cube. It is important to choose the gap value that provides the best results and facilitates production and integration. The scattering parameters simulated by varying the gap between the outer cube and the inner cylinder are given in Fig. 8. In this study, the electrical targets of the design are as follows: insertion loss $<$0.05 dB, return loss $>$30 dB, and isolation $>$80 dB. For mechanical constraints, the manufacturing tolerance should be on the order of 0.02 mm. A gap of 0.04 mm between the inner cylinder and the outer cube is required for a shrink fit of the inner cylinder into the cavity inside the outer cube. Therefore, the optimum gap value of 0.06 mm is chosen for good electrical performance of the switch and ease of fabrication and assembly. Unlike [19], the gap-waveguide pin structure in this work is directly integrated along the cylindrical rotor interface, where leakage is most critical during rotation. This configuration enables stronger field confinement and is a key factor in achieving the reported wideband and high-isolation performance.

Based on the simulations, the design parameters for the waveguide switch are given in Table 1.

Table 2. Scattering parameters for simulation and measurement

	Return loss (dB)	Insertion loss (dB)	Isolation (dB)
Simulation	$>$33	$<$0.06	$>$155
Measurement	$>$30	$<$0.1	$>$90

Measurement

The designed waveguide switch is manufactured from aluminum. The inner cylinder was produced in two separate parts and assembled with bolts. Bearings are added to the top and bottom of the inner cylinder to ensure rotation. The inner cylinder is positioned in the cavity of the outer cube by shrink fitting. The outer layer was produced in three separate parts: the outer cube, the actuating mechanism, and the cover. These parts are connected with bolts.

The scattering parameters of the mechanical waveguide switch are measured with a two-port vector network analyzer. While measuring the scattering parameters between two ports, the other ports were terminated with a matched load. The measurement setup is shown in Fig. 9.

The scattering parameters of the designed and fabricated waveguide switch are given in Table 2 and Fig. 10. The scattering parameter results of the designed switch are in agreement with the measurement results of the manufactured switch.

Table 3 compares the proposed switch with previously reported waveguide switch designs. As shown in the table, the proposed switch provides the widest bandwidth, covering the entire X-band. While the insertion loss (IL) performance is comparable to that of existing designs, the proposed structure achieves improved return loss (RL) and isolation (Iso.). In particular, the proposed design provides a return loss above 30 dB and an isolation above 90 dB, whereas previously reported designs typically exhibit return loss values below 20 dB and isolation levels below 60 dB [16, 19]. These results demonstrate the improved RF performance achieved by the proposed switch. It should also be noted that, unlike the design presented in [19], the proposed switch employs a gap-waveguide-based structure with a dedicated actuator mechanism, enabling improved RF performance and wideband operation.

RF breakdown analysis

A system used in high-frequency, high-power applications is expected to transmit a high-power signal. The inability of the system to withstand a high-power signal, which can damage the structure and prevent transmission, is called RF breakdown or

https://doi.org/10.1017/S1759078726103638 Published online by Cambridge University Press

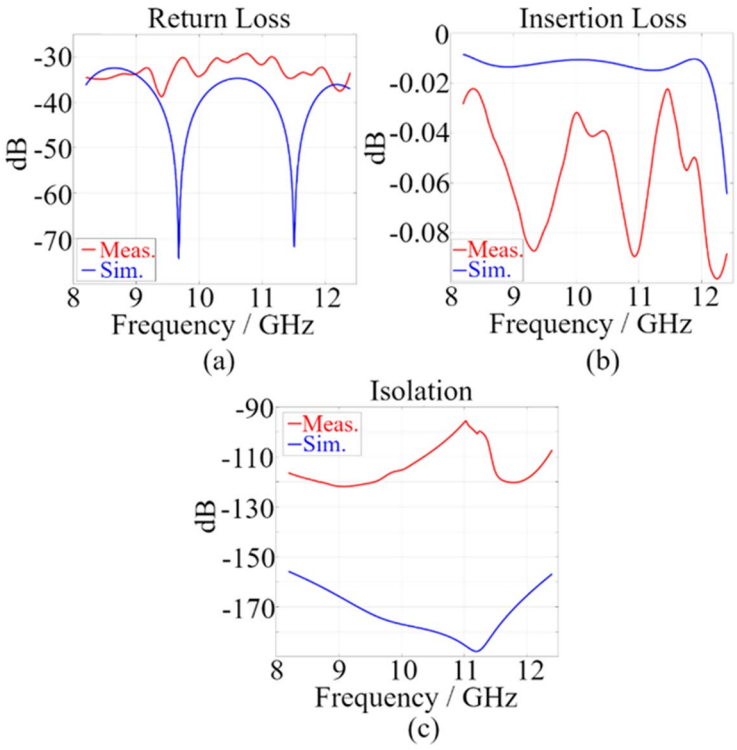


Figure 10. Scattering parameters for simulation and measurement: (a) Return loss. (b) Insertion loss. (c) Isolation.

Table 3. RF performance comparison between the proposed switch and previously reported waveguide switches

	FB	BW (%)	IL (dB)	RL (dB)	Iso. (dB)
This work	X	40.78	0.1	30	90
[16]	Ku	25.45	0.8	10	25
[18]	Ku	10.91	1.5	20	40
[19]	Ku	25	0.1	20	60

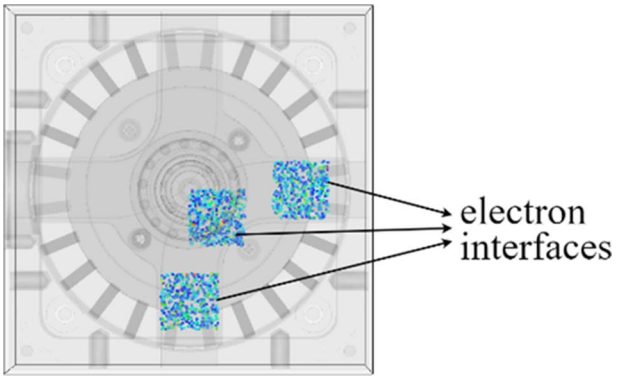


Figure 11. Electron interfaces on the transmission of the switch.

electrical breakdown. RF breakdown can be explained by corona discharge and multipacting.

The corona effect occurs naturally in high-power applications because air, which contains many free electrons and ions under normal conditions, is not a perfect insulator. When an electric field passes through the air between two conductors, electrons on the surface of the conductor are ejected if they reach sufficient energy. Under the influence of the electric field, free ions and electrons in the air are exposed to a force. As a result, ions and free electrons accelerate. During their movement, charged particles collide with each other and with slow-moving uncharged molecules. Thus, the number of charged particles increases rapidly. If the electric field strength between electrons is strong enough, the interactions between electrons become non-negligible. The strength of the electric field causes electrons to break away from the conductors and the air surrounding the conductors to dissociate into ions. This makes the air conductive, leading to arcing between the conductors [25].

Electron multipacting is a phenomenon in vacuum tubes and waveguides to which RF and high-power signals are applied, in which, under certain conditions, the emission of secondary electrons in resonance with an electric field leads to exponential electron multipacting, damaging or even destroying the RF device. This is especially important to consider in high-power space applications.

When electrons, accelerated by an electric field in a cavity, hit the surface of this cavity, they eject electrons from the surface. The accelerated electrons are called "primary electrons," and the electrons removed from the surface by the primary electrons are called "secondary electrons." Depending on the impact, energy, and angle of the primary electron on a surface, the cavity can release one or more secondary electrons into the vacuum. These electrons can then be accelerated by electric fields and hit the same or another surface. If the energy and frequency of the electric field increase, the number of electrons ejected increases, leading to a multipacting effect [26]. When the number of free electrons in the medium reaches a non-negligible level, the medium becomes conductive. In prolonged electron multipacting, the structure can be physically damaged. It is therefore important to perform high-power testing of components.

https://doi.org/10.1017/S1759078726103638 Published online by Cambridge University Press

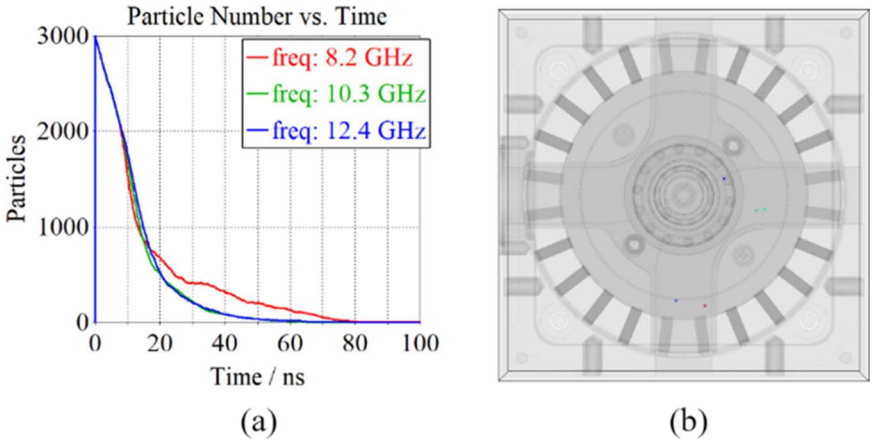


Figure 12. The number of primary and secondary electrons (a) versus time (b) on the structure (100 kW).

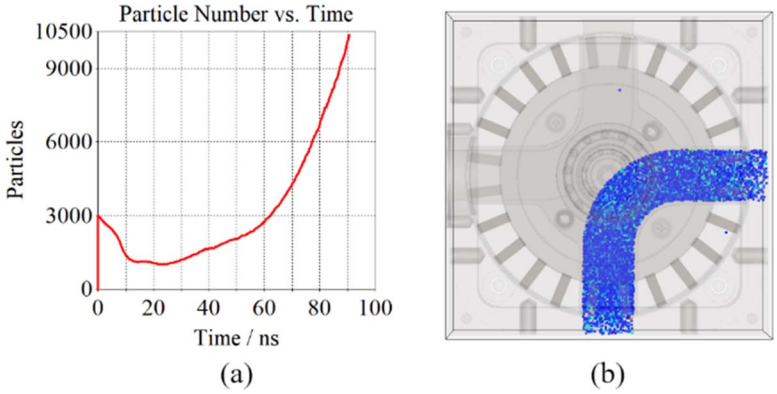


Figure 13. The number of primary and secondary electrons (a) versus time (b) on the structure (125 kW).

Table 4. Actuator design limits

Parameter	Value
Rotation time	50 ms
Actuator current	0.9 A
Actuator voltage	28 V

Multipacting depends on the material used in the system. Secondary electron emission (SEE) is a high-power parameter that varies with material. The Vaughan and Furman models are the two main models for SEE-type materials.

In this study, multipactor analysis is used as a design verification tool to evaluate the switch's high-power endurance rather than performing a detailed parametric multipactor investigation. Analysis is performed using the particle-in-cell template in the Particle Studio package within the commercial CST program to assess the switch's high-power endurance. For the multipacting simulation, the switch's building material is selected as "SEE-Aluminum," which exhibits SEE. To analyze the effect of primary electrons on the structure, three distinct primary-electron interfaces are defined along the electric-field transmission path. As shown in Fig. 11, 1000 electrons are assigned to each electron interface, for a total of 3000 electrons.

In total, 100 kW of power is applied to the switch for 100 ns. Primary electrons hit the surfaces at power levels below 100 kW. If the structure can withstand this power, no multipacting occurs, and the number of electrons decreases over time. The sum of the primary and secondary electron numbers is called particle number, and the particle number versus time is given in Fig. 12(a). The electrons on the structure at the end of 100 ns are also shown in Fig. 12(b).

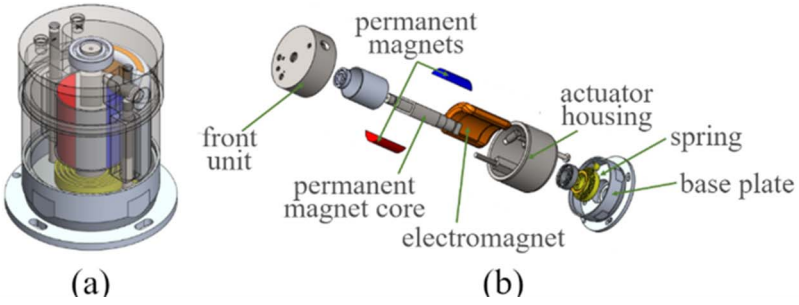


Figure 14. The integrated actuator mechanism (a) with the transparent view and (b) with flat-looking structure.

https://doi.org/10.1017/S1759078726103638 Published online by Cambridge University Press

Table 5. Actuator components with their materials

Parameter	Value (mm)
Front unit	Stainless steel
Permanent magnet	Samarium cobalt
Electromagnet core	Soft iron
Housing	Soft iron
Permanent magnet core	2Cr13
Return spring	Stainless steel
Base plate	Aluminum

As seen in Fig. 12, the number of electrons inside the switch decreases over time. Based on the simulations, it was concluded that the structure can withstand the desired power of 100 kW and that there is no RF breakdown within it. The structure can withstand 100 kW; however, analyses were performed to determine the power at which the structure experiences RF breakdown. The analysis determined that the structure cannot withstand 125 kW of power. The particle number versus time for 125 kW is given in Fig. 13(a). The electrons on the structure at the end of 90 ns are also shown in Fig. 13(b).

As shown in Fig. 13, the number of particles increased rapidly over the first 90 ns. That is, electron multipacting occurred on the switch transmission path. The switch cannot withstand 125 kW power.

Actuating mechanism

In the waveguide switch used in high-power communication systems, rotary movement between the RF transmission lines is achieved via a rotary actuator with an electromechanical operating mechanism. The actuator analysis presented in this section focuses on the design methodology and the estimation of the required torque and switching time for the proposed waveguide switch. The actuator mechanism simulations were carried out using COMSOL Multiphysics (COMSOL AB). In addition, the mechanical parameters of the rotating structure, such as the moment of inertia, were obtained using SolidWorks [27]. Providing high torque in milliseconds, it typically has a structure that includes permanent magnets, coil, outer and inner housings, and other mechanical fasteners [28]. The limits of the developed waveguide switch actuator mechanism are given in Table 4.

The actuator mechanism is designed to be failsafe, returning to its starting position when the power is cut off. The transparent appearance and flat structure of the integrated actuator mechanism are shown in Fig. 14.

The actuator's rotation is enabled by the magnetic circuit formed by the coil, permanent magnets, and high-permeability materials. A core material with high magnetic permeability holds the permanent magnets together, and the rotation torque is transferred to the waveguide via this shaft. There is a coil and two permanent magnets inside the structure. The main magnetic circuit is completed through these elements. In addition, a spiral spring provides the structure's failsafe feature, along with a spring guide that surrounds it. The remaining elements were selected based on the need for magnetic permeability, the BH curve for completing the magnetic circuit, and the mechanical fixation of the structure [28]. The materials for the actuator components are defined in Table 5.

Considering the specifications of the waveguide switch, the amount of torque needed to perform the rotation movement in the desired time is obtained with a formulation [29]:

$$\tau = I * \omega = I * \frac{2\theta}{t^2} \tag{1}$$

where τ is torque, I is inertia, ω is angular velocity, θ is rotation angle, and t is rotation time. τ of ~6.27 Ncm is required to switch a waveguide with I of 49,918 gmm^2 (obtained from SolidWorks) under 50 ms in theoretical approach. θ is obtained from the derivative of the angular velocity. Moreover, actuator simulation was primarily performed by defining the number of coil windings, the conductor wire diameter, the BH curves of the hard and soft magnetic materials used, the residual magnetization, the magnetic permeability, and the coil voltage. The simulation parametric context structure is given by the black-box model in Fig. 15. The simulation results are evaluated with respect to the electromagnet current, rotation time, and rotation angle.

The simulations are carried out in COMSOL Multiphysics. COMSOL is a software that simulates structures in applications such as acoustics, electromagnetics, chemical reactions, mechanics, fluid flow, and heat transfer by solving Maxwell's equations. In this study, to obtain the best results for the actuator mechanism, several designs, including double- and single-coil and inner-outer rotor configurations, are evaluated. According to the simulation results, the best solution to achieve the failsafe mode is the single-coil, inner-rotor drive mechanism.

Figure 16 shows the BH graph for soft iron, the most commonly used material for magnetic circuit design in this kind of

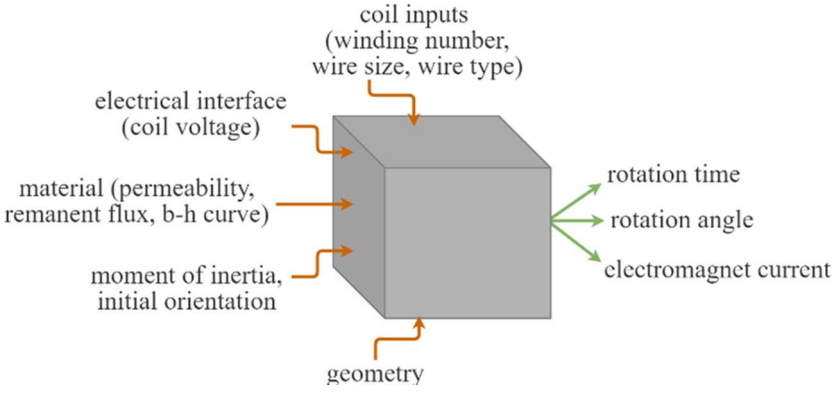


Figure 15. Black-box model for parametric relation of the actuator simulation.

https://doi.org/10.1017/S1759078726103638 Published online by Cambridge University Press

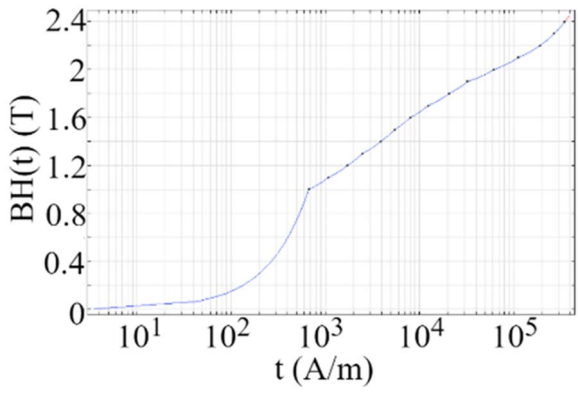


Figure 16. BH graph for soft iron.

application. Since it requires a small A/m to reach a high magnetic field, compared to other high-permeability materials like nickel alloys or low-carbon steel. In this actuator, the electromagnet core and housing are made of soft iron.

The magnetic field required to initiate rotation is related to the number of windings and the coil current. The coil is designed with the wire depending on the current capacity and coil core. Figure 17(a) shows the current through the wires over time for different winding numbers. Regardless of the number of windings and wire types, the volume the coil will occupy is the same in each scenario. The purpose of this analysis is to determine a suitable winding number regarding wire current capacity. American wire gauge (AWG) is a standard that numbers wires by size. After many attempts with different AWG wire sizes, AWG 37 wire, with a maximum current capacity of 22 mA, is used in this design. As seen in Fig. 17(b), except for 10,000 winding numbers, the other winding numbers exceed the maximum current capacity while the actuator reaches 90° of rotation. In the graph, 10,000 windings of wire draw a current of ±20 mA. A 0.8 T magnet is used in this simulation.

The remaining part of the analysis was performed with a winding number of 10,000. The second part of the study was determined by the residual magnetization parametric approach applied to the selected permanent magnet in the simulation to select the permanent magnet type. Accordingly, a 0.8 T residual magnetized permanent magnet offers the best solution in terms of rotation time and coil current.

As shown in Fig. 18(b), as the magnet's remanent flux increases, the time required for a 90° rotation decreases. Figure 18(a) shows the current drawn by the coil wire as a function of different remanent flux values. The selected AWG 37 wire can withstand a maximum current of 20 mA. When Fig. 18(a) and (b) are analyzed together, a 0.8 T magnet is chosen so that the current passing through the wire is less than 20 mA and the switching time is close to 20 ms.

The actuator design in this study uses a Samarium Cobalt magnet (YX-16) because of its superior temperature resistance. Figure 19 shows the temperature-related residual flux characteristic of this magnet.

The torque amounts depending on time are given in Fig. 20 with the latest design structure decided. The graph shows that 14 Ncm values are reached. This value meets the 6.4 Ncm value required for switching as calculated in (1).

Final design decisions are given in Table 6 for the rotary actuator of the waveguide switch.

Conclusion

Compared to previously reported waveguide switch structures, the proposed design offers a unique combination of GWT and integrated actuation, enabling contactless high-power operation with faster switching time and improved electrical performance. This

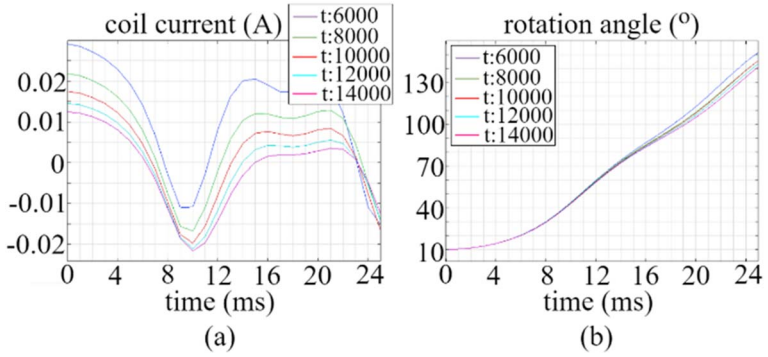


Figure 17. Time-dependent (a) coil current and (b) rotation angle of the actuator for different coil winding numbers (t).

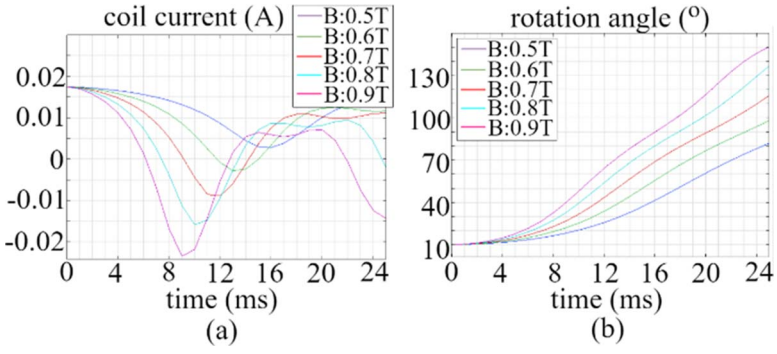


Figure 18. Time-dependent (a) coil current and (b) rotation angle of the actuator for different permanent magnet fluxes (B).

https://doi.org/10.1017/S1759078726103638 Published online by Cambridge University Press

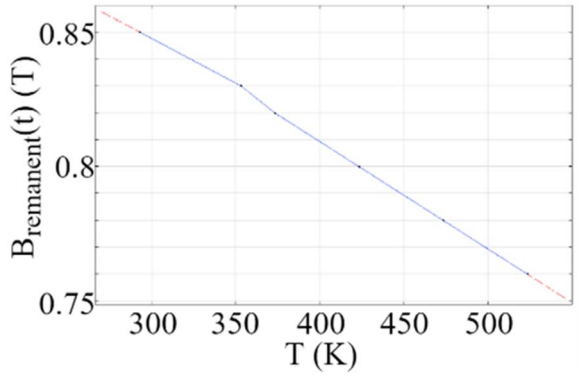


Figure 19. Temperature-related remanent flux characteristic for Samarium Cobalt YX-16.

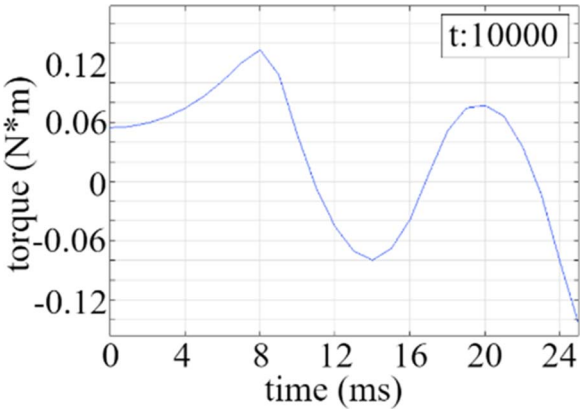


Figure 20. Time-dependent torque of the actuator for 10,000 turns.

Table 6. Final parameters of the actuator mechanism

Parameter	Value (mm)
Coil turn number	10,000
Permanent magnet	Samarium cobalt YX-16
Wire size	0.10 mm
Coil voltage	28 V
Permanent magnet core	2Cr13
Return spring	Stainless steel 302
Base plate	Aluminum

paper presents the design of DPDT and SPDT mechanical waveguide switches for high-power X-band applications. The switch structure consists of a rotatable inner cylinder and a fixed outer cube, with no physical contact between them, ensuring ease of assembly and improved durability. The design can withstand up to 100 kW of peak power. The fabricated prototype has been tested and shows strong agreement with the simulation results, achieving a return loss greater than 30 dB, an insertion loss below 0.1 dB, and an isolation above 90 dB. The switching mechanism is controlled by a custom-designed rotary actuator, and the actuator is designed to achieve a switching time below 50 ms when operated under a 28 V supply.

Funding statement. This study was supported by TUBITAK under project number 119C032.

Competing interests. The authors declare none.

References

1. **Kildal P, Alfonso E, Valero-Nogueira A and Rajo-Iglesias E**. (2009) Local metamaterial-based waveguides in gaps between parallel metal plates. *IEEE Antennas and Wireless Propagation Letters* **8**, 84–87. https://doi.org/10.1109/LAWP.2008.2011147
2. **Rahiminejad S, Pucci E, Vassilev V, Kildal PS, Haasl S and Enoksson P**. (2016) Polymer gap adapter for contactless, robust, and fast measurements at 220-325 GHz. *Journal of Microelectromechanical Systems* **25**(1), 160–169. https://doi.org/10.1109/JMEMS.2015.2500277
3. **Sun D, Chen Z and Xu J**. (2016) Flexible rectangular waveguide based on cylindrical contactless flange. *Electronics Letters* **52**(25), 2042–2044. https://doi.org/10.1049/el.2016.3536
4. **Cui W, Chen X, He Y and Sun D** (2019) A compact waveguide connection for space applications using gap waveguide technology. In *2019 13th European Conference on Antennas and Propagation (EuCAP)*. Krakow, Poland.
5. **Cui W, Chen X, Sun D and He Y** (2020) Flangeless waveguide connection based on gap waveguide technology. In *2020 14th European Conference on Antennas and Propagation (EuCAP)*. Copenhagen, Denmark.
6. **Alos EA, Zaman AU and Kildal P-S**. (2013) Ka-band gap waveguide coupled-resonator filter for radio link diplexer application. *IEEE Transactions on Components, Packaging and Manufacturing Technology* **3**(5), 870–879. https://doi.org/10.1109/TCPMT.2012.2231140
7. **Padilla P, Palomares-Caballero A, Alex-Amor A, Valenzuela-Valdes J, Fernandez-Gonzalez JM and Quevedo-Teruel O**. (2019) Broken glide-symmetric holey structures for bandgap selection in gap-waveguide technology. *IEEE Microwave and Wireless Components Letters* **29**(5), 327–329. https://doi.org/10.1109/LMWC.2019.2906460
8. **Ahmadi B and Banai A**. (2015) Direct coupled resonator filters realized by gap waveguide technology. *IEEE Transactions on Microwave Theory and Techniques* **63**(10), 3445–3452. https://doi.org/10.1109/TMTT.2015.2457916
9. **Alfonso E, Zaman AU, Pucci E and Kildal PS** (2012) Gap waveguide components for millimetre-wave systems: Couplers, filters, antennas, MMIC packaging. In *International Symposium on Antennas and Propagation*. Nagoya, Japan.
10. **Guo M and Yang F** (2020) W-band dual polarized array antenna based on gap waveguide technology. In *Asia-Pacific Microwave Conference*. Hong Kong.
11. **Ahmadi B and Banai A** (2016) A power divider/combiner realized by ridge gap waveguide technology for millimeter wave applications. In *Fourth International Conference on Millimeter-Wave and Terahertz Technologies*. Tehran, Iran.
12. **Zaman AU, Alexanderson M, Vukusic T and Kildal PS**. (2014) Gap waveguide PMC packaging for improved Isolation of circuit components in high-frequency microwave modules. *IEEE Transactions on Components, Packaging and Manufacturing Technology* **4**(1), 16–25. https://doi.org/10.1109/TCPMT.2013.2271651
13. **Ahmadi B and Banai A**. (2016) Substrateless amplifier module realized by ridge gap waveguide technology for millimeter-wave applications. *IEEE Transactions on Microwave Theory and Techniques* **64**(11), 3623–3630. https://doi.org/10.1109/TMTT.2016.2607177
14. **Farahbakhsh A**. (2021) Wideband rotary joint based on gap waveguide technology. *IEEE Transactions on Microwave Theory and Techniques* **69**(10), 4385–4391. https://doi.org/10.1109/TMTT.2021.3090988
15. **Varadan VK, Vinoy KJ and Jose KA** (2003) *Switches for RF and Microwave Applications*. Hoboken, NJ: Wiley.
16. **Ruiz-Cruz JA, Fahmi MM and Mansour RR**. (2011) Generalized multiport waveguide switches based on multiple short-circuit loads in power-divider junctions. *IEEE Transactions on Microwave Theory and Techniques* **59**(12), 3347–3355. https://doi.org/10.1109/TMTT.2011.2170089

https://doi.org/10.1017/S1759078726103638 Published online by Cambridge University Press

17. **Shishido T, Eyermann PA, Vick WL and Cramm HW**, Four port waveguide switch. U.S. Patent 922,895, 30 December 1980.
18. **Ruiz-Cruz JA, Fahmi MM and Mansour RR** (2014) Single-pole multiple-throw waveguide switch for twelve output ports (SP12T). In *Proceedings of the 44th European Microwave Conference*. Rome, Italy.
19. **Tayebpour J, Ahmadi B, Fallahzadeh M, Shekoo O and Torabi A**. (2019) A waveguide switch based on contactless gap waveguide technology. *IEEE Microwave and Wireless Components Letters* **29**(12), 771–774. https://doi.org/10.1109/LMWC.2019.2950164
20. **Silveirinha M, Fernandes C and Costa J**. (2008) Electromagnetic characterization of textured surfaces formed by metallic pins. *IEEE Transactions on Antennas and Propagation* **53**(6), 405–415. https://doi.org/10.1109/TAP.2007.915442
21. **Rajo-Iglesias M and Kildal PS**. (2011) Numerical studies of bandwidth of parallel plate cut-off realized by bed of nails, corrugations and mushroom-type EBG for use in gap waveguides. *IET Microwaves, Antennas & Propagation* **5**(3), 282–289. https://doi.org/10.1049/iet-map.2010.0073
22. **Kildal PS** (2009) Three metamaterial-based gap waveguides between parallel metal plates for mm/submm waves. In *Proceedings of the European Conference on Antennas and Propagation*.
23. **Kildal PS, Zaman A, Rajo-Iglesias E, Alfonso E and Valero-Nogueria A**. (2011) Design and experimental verification of ridge gap waveguide in bed of nails for parallel-plate mode suppression. *IET Microwaves, Antennas & Propagation* **5**(3), 262–270. https://doi.org/10.1049/iet-map.2010.0089
24. **Systèmes D**. CST studio suite 2024, Computer Simulation Technology, version: 2021.05 (June 28, 2021). Available at https://www.3ds.com/products-services/simulia/products/cst-studio-suite/ (accessed June 2025).
25. **Veldhuizen EM and Rutgers WR** (2001) Corona discharges: Fundamentals and diagnostics. *Low Temperature Plasma Diagnostics* **3**, 40–49.
26. **Sounas A** (2015) Modeling of long-term multipactor evolution in microwave components including dielectric layers. *Ecole Polytechnique Federale Lausanne*, pp. 113–178.
27. **COMSOL AB**. COMSOL Multiphysics®, Stockholm, Sweden. Available at https://www.comsol.com/comsol-compiler (accessed June 2025).
28. **Microwave D-K**. Design Guide Microwave Switches & RF Coaxial Relays. Available at https://www.everythingrf.com/whitepapers/details/118-design-guide-microwave-switches-amp-rf-coaxial-relays (accessed 03 May 2024).
29. **SMC**. Rotary actuators model selection. Available at https://ca01.smcworld.com/catalog/SMC-HP-PDF/ro_actuator_select-en.pdf (accessed 03 May 2024).



Merve Güvenç received the B.Sc. degree in electrical and electronics engineering from Yeditepe University, Istanbul, Turkey, in 2020. She started her Ph.D. after completing her M.Sc. at Yeditepe University in 2020. She has been working as an RF design engineer at Profen Technologies since 2020. Her current research interests include computational electromagnetics, RCS measurements, electromagnetic analysis, design of high-power antennas, and communication systems components.



Çağlar Konak was born in Istanbul, Turkey, in 1991. He received both the B.Sc. and M.Sc. degrees in physics from Middle East Technical University, Ankara, Turkey, in 2015 and 2019, respectively. Between 2015 and 2019, he participated in the AMS Collaboration at CERN, focusing on understanding the space radiation environment through the proton spectrum and the effects of solar modulation. He is interested in finite element analysis, precision cleaning and packaging, beam and material interactions, vacuum tube conditioning setups, and electromagnetic actuator mechanisms for communication systems.



İsmail Şişman was born in Istanbul. He received his bachelor's and master's degrees in electronics and communication engineering from Haliç University in 2009 and 2011, respectively. He completed his Ph.D. degree in electrical and electronics engineering at Yeditepe University. He worked as a Research Assistant at the Electrical and Electronics Engineering Department of Haliç University between 2009 and 2012, and as a Research Assistant at Yeditepe University between 2012 and 2017. Since 2017, he has been working as RF Group Manager at the R&D Centre of PROFEN Technologies, a company operating in the satellite communication sector.



A. Arif Ergin was born in Ankara, Turkey, in 1970. He received the B.Sc. degree in electrical and electronics engineering from the Middle East Technical University, Ankara, Turkey, in 1992, and the M.Sc. and Ph.D. degrees in electrical and computer engineering from the University of Illinois at Urbana-Champaign, Urbana, in 1995 and 2000, respectively. Between 2000 and 2016, he was with the Electronics Engineering Department, Gebze Technical University. He also assumed part-time positions on various projects in TÜBITAK. Between 2014 and 2015, he served as the President of TÜBİTAK Informatics and Information Security Research Center. Between 2015 and 2018, he was the President of TÜBİTAK. Since 2024, he has been with the Bahçeşehir University, Electric and Electronics Engineering Department. He is interested in numerical analysis, simulation, and measurement of electromagnetic wave phenomena.

https://doi.org/10.1017/S1759078726103638 Published online by Cambridge University Press